Determining Parameters of Metal-Halide Perovskites Using Photoluminescence with Bayesian Inference

Manuel Kober-Czerny, Akash Dasgupta, Seongrok Seo, Florine M. Rombach, David P. McMeekin, Heon Jin, and Henry J. Snaith*

Department of Physics, University of Oxford, Clarendon Laboratory, Parks Road, Oxford, OX1 3PU, United Kingdom

(Received 24 May 2024; revised 27 November 2024; accepted 4 December 2024; published 14 January 2025)

In this work, we demonstrate that time-resolved photoluminescence data of metal halide perovskites can be effectively evaluated by combining Bayesian inference with a Markov-chain Monte-Carlo algorithm and a physical model. This approach enables us to infer a high number of parameters that govern the performance of metal halide perovskite-based devices, alongside the probability distributions of those parameters, as well as correlations among all parameters. Via studying a set of halfstacks, comprising electron- and hole-transport materials contacting perovskite thin films, we determine surface recombination velocities at these interfaces with high precision. From the probability distributions of all inferred parameters, we can simulate intensity-dependent photoluminescence quantum efficiency and compare it to experimental data. Finally, we estimate mobility values for vertical charge-carrier transport, which is perpendicular to the plane of the substrate, for all samples using our approach. Since this mobility estimation is derived from charge-carrier diffusion over the length scale of the film thickness and in the vertical direction, it is highly relevant for transport in photovoltaic and light-emitting devices. Our approach of coupling spectroscopic measurements with advanced computational analysis will help speed up scientific research in the field of optoelectronic materials and devices and exemplifies how carefully constructed computational algorithms can derive valuable plurality of information from simple datasets. We expect that our approach can be expanded to a variety of other analysis techniques and that our method will be applicable to other semiconductors.

DOI: 10.1103/PRXEnergy.4.013001

I. INTRODUCTION

The photovoltaic performance of the most efficient metal halide perovskite-based solar cells are within 80% of the detailed balance limit [1–4]. Understanding the origin of performance losses is now crucial for making the final advances in efficiency and to sustain performance over years and decades of operation. However, more losses exist in wide-band-gap perovskite cells, which are required for highly efficient multijunction cells, necessitating a better understanding of losses in these materials and devices. In this context, perovskite thin films are commonly studied to understand the degradation of the material itself, while "half-stacks," a reduced selection of layers from the multilayer device stacks, are used to understand the impact of interfaces and interfacial losses. A common methodology to study these interfaces is to assess the photoluminescence (PL) via photoluminescence quantum efficiency [5–7] (PLQE) and time-resolved photoluminescence [8,9] (TRPL) measurements.

For TRPL, the sample is illuminated by a short laser pulse and the PL is measured and recorded in a time-correlated manner. The PL intensity typically decays over a time period of nanoseconds to tens of microseconds after the pulsed excitation. An initial fast drop, often observed, has been ascribed to early-time diffusion [10–12], trap filling of shallow defects [13,14], and spatial heterogeneity [15] in the optoelectronic properties of the material. The shape of the decay can thus give insights into material properties to varying complexity, but it is usually difficult to disentangle the different processes responsible for PL decay. The most common and simplest approaches are to use either a biexponential decay, from which two lifetimes can be extracted, or a stretched exponential decay, from which a lifetime and stretching factor can be extracted [15–18]. In some exceptional cases, a triexponential [19,20] decay has been used, where physical meaning was given to all three extracted lifetimes. This can lead to confusing and even contradictory interpretations of results.

*Contact author: henry.snaith@physics.ox.ac.uk

The simplest physical model for charge-carrier recombination is the continuity equation without drift or diffusion:

$$\frac{d\Delta n(t)}{dt} = -k_1\Delta n(t) - k_2\Delta n(t)^2 - k_3\Delta n(t)^3, \quad \mathrm{PL}(t) \propto k_2\Delta n(t)^2, \tag{1}$$

where k_1, k_2, and k_3 are linked to mono-, bi-, and trimolecular recombination processes, respectively; $\Delta n(t)$ is the photogenerated charge-carrier density as a function of time; and $I_{\mathrm{PL}}(t)$ is the PL that is measured as a function of time. Analytical solutions have been described; however, it can also be solved numerically and fitted to data using a least-squares approach. With this model, a set of TRPL measurements with changing Δn, achieved by varying laser fluences, can be used to accurately extract physically meaningful recombination parameters. Still, the model is a gross simplification and the dynamics of the early-time decay of the PL trace, as well as the heterogeneity of parameters, cannot be captured by this model.

To further our understanding of the processes that govern the transient PL behavior in metal halide perovskites, we can formulate a model that includes diffusion and recombination via shallow defects using eight device-relevant parameters [μ_{vert}, the vertical (or out of plane of the substrate) mobility; k_{c} and k_{e}, the rates of electron capture into and emission from a shallow defect, respectively; k_{d}, the nonradiative recombination rate via a deep bulk defect; k_{rad}, the radiative recombination constant; S_{top} and S_{bot}, the surface recombination velocities at the top and bottom interfaces, respectively; p_{eq} the equilibrium hole density under pulsed excitation (which could interchangeably be electron density if we assumed that holes were the predominantly trapped carrier type)] to describe the TRPL response. However, this large parameter space can result in a nonidentifiable model (often wrongly termed "overfitted"), meaning there are multiple degenerate solutions that describe the observations equally well.

Here, we use Bayesian statistics to mitigate these limitations of applying a multiparameter model. Each parameter is described by a probability distribution rather than a single value. Initial knowledge about a parameter is encoded into a *prior* distribution (it can be a uniform distribution if no prior knowledge is present). A set of values for each parameter known as a *sample* is drawn from the *prior*. Based on these parameters, the model is evaluated and the resulting simulated TRPL trace is compared to experimental data with the help of a *likelihood* function. It determines how well the parameters describe the data based on the physical model. Bayes' theorem [21],

$$P(A|B) = \frac{P(B|A)P(A)}{P(B)}, \tag{2}$$

where $P(B|A)$ is the conditional probability of B occurring, given A (*likelihood*), and $P(A)$ and $P(B)$ are the unconditional probabilities of observing A (*prior*) and B (*data*), which can be used to estimate the *posterior* distribution [$P(A|B)$, the conditional probability of A occurring, given B] of the parameter after data have been assessed. To reduce the computational demands, in this work, we use a Markov-chain Monte-Carlo algorithm to select random samples from the prior distribution of the parameters. We call the combination of Bayesian inference and Markov-chain Monte-Carlo (MCMC) algorithm, the "Bayes-MCMC" approach. In Fig. 1 we show a schematic of the Bayes-MCMC algorithm. In short, the MCMC algorithm picks a random sample of parameters from the prior distribution. For each pick, the entire TRPL decay is calculated from our physical model. Then, the experimental data are compared to the calculation and assigned a likelihood (between 0 and 1). If the likelihood is larger than a random number generated by the MCMC, then the parameters are stored, otherwise they are discarded. A new combination of parameters (*sample*) is drawn. Over many iterations, the stored samples will generate the posterior distributions for each parameter. In theory, this approach is not limited to a certain number of parameters, but the outcome is determined by the number of available data points and MCMC steps. This approach was previously utilized on limited sets of measurements, and the total time of calculation was quite long (multiple tens of hours) [23,24] due to the use of an MCMC algorithm following the classic implementation of Metropolis and Hastings [25]. In our work, we improve upon this by making use of more modern state-of-the-art gradient-based MCMC algorithms, namely, the "no-U-turn" (NUTS) [26] sampler ("PyMC" library [22]). Gradient-based MCMC samplers explore the posterior distributions much more efficiently. Instead of $>10^3$ steps, the gradient-based samplers can achieve convergence of multiple chains within only 10^3 samples. For this work, we use the NUTS sampler with 10^3 tuning steps, during which the parameters of the sampler (such as the step size) are optimized, as well as 10^3 steps that are stored for later use. The time of a typical calculation was cut down to less than 2 h on a professional grade workstation or 2–3 h on a consumer quad-core mobile CPU.

We initially tested our approach on a set of TRPL data from formamidinium lead iodide ($FAPbI_3$) thin films on glass to disentangle the different processes that affected the early-time decay, and then we extended our approach to study half-stacks comprising $FAPbI_3$ thin films interfaced with the electron-transport material SnO_2 or the hole-transport material 2,2′,7,7′-tetrakis[*N*,*N*-di(4-methoxyphenyl)amino]-9,9′-spirobifluorene (Spiro-OMeTAD) to understand the influence of interface recombination. Losses at heterojunctions are key limiting factors in solar cell performance, and engineering the surface to passivate defects has been the topic of the most recent works that claim the highest efficiencies in photovoltaic cells [27,28]. The assessment of half-stacks is not

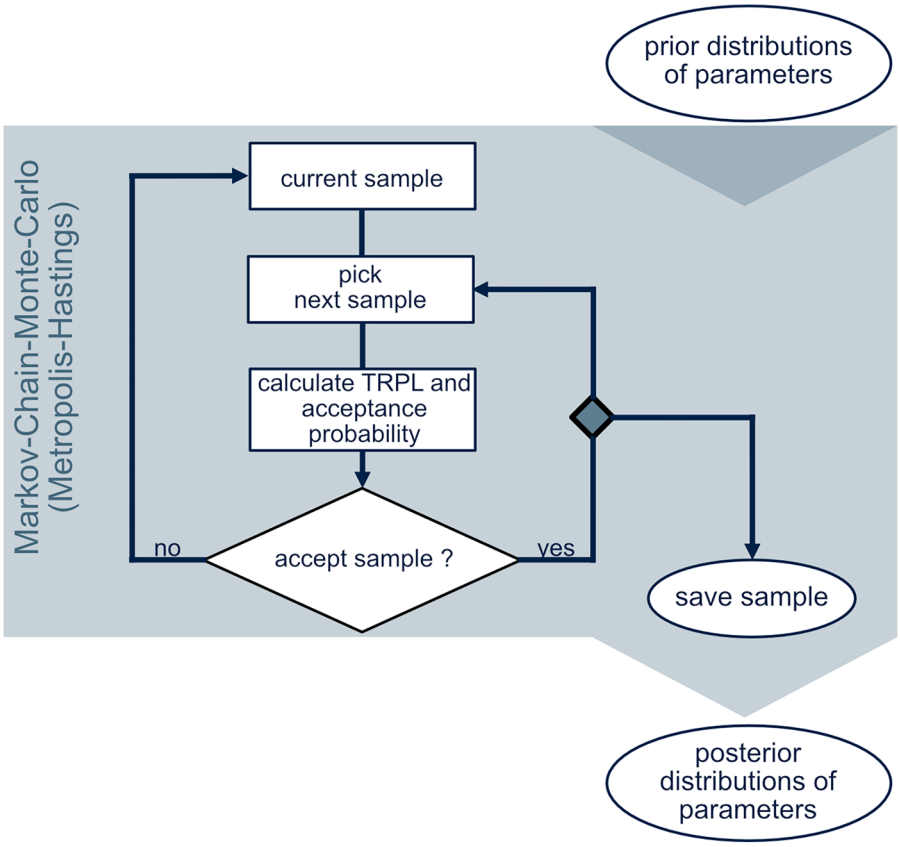

FIG. 1. Schematic of the Bayes-MCMC algorithm. Each parameter is defined by a prior distribution, which encodes the knowledge about them (for example, each parameter used in this work needs to be >0; see SI.4 in the Supplemental Material [36] for more details). Markov-chain Monte-Carlo algorithm (here, a Metropolis-Hastings algorithm is used) picks a random sample from the prior distribution of each parameter. Corresponding TRPL decay is calculated, and an acceptance probability is determined based on Eq. (2). Sample is only accepted, if the acceptance probability is larger than a random threshold value (optimized by the PyMC's NUTS sampler [22]). Upon acceptance, the sample is saved, and a new sample is randomly selected. Over time, the saved samples will approximate the posterior distribution in the multidimensional parameter space.

a simple task, and usually the number of free parameters needs to be reduced by fixing some of them to known values from other experiments. For instance, to assess a half-stack, a "bare" perovskite thin film on glass can be used to determine the "bulk recombination" parameters (assuming that the surface recombination is negligible) first. Then a half-stack is measured and the difference in recombination is assigned to the newly introduced interface [8,29–31]. This is a viable approach to get an estimate of the surface recombination; however, it has some limitations in the case of perovskite materials, as the underlying layer can affect the crystallization and final film morphology, which, in turn, will affect the bulk and surface properties and recombination parameters [32,33]. Our methodology, with the complete physical model, allows us to measure these samples directly. The results give insights into the underlying optoelectronic mechanisms that govern the transient charge-carrier behavior in these samples.

II. THE PHYSICAL MODEL

The main aims of the methodology we have developed are to differentiate between early-time trapping and charge-carrier diffusion in the TRPL response of perovskite thin films, and to disentangle interface and bulk recombination in half-stack stacks and complete devices. The model described here builds upon work from Maiberg *et al.* [34,35]. To estimate the time-resolved PL behavior in any semiconductor, the radiative recombination rate needs to be calculated. Assuming homogeneity in the x-y plane, the time-resolved PL response [$\mathrm{PL_{obs}}(t)$] is

$$\mathrm{PL_{obs}}(t) \propto \int_0^d R_{\mathrm{rad}}(t,z)dz \; + \; \varepsilon_{\mathrm{PL}};\; \varepsilon_{\mathrm{PL}} < 0.01\mathrm{PL_{obs}}\,, \tag{3}$$

where R_{rad} is the total radiative recombination rate, d is the film thickness, and $\varepsilon_{\mathrm{PL}}$ is the noise floor of the TRPL

measurement. The total radiative recombination rate can be written as

$$R_{\mathrm{rad}}(t,z) = k_{\mathrm{rad}}\Delta n(t,z)(\Delta p(t,z) + p_{\mathrm{eq}}), \tag{4}$$

where k_{rad} is the radiative recombination rate constant; $\Delta n(t,\ z)$ and $\Delta p(t,\ z)$ are the photogenerated electron- and hole concentrations, respectively, as a function of time t and film z-coordinate; and p_{eq} is the equilibrium or background charge-carrier concentration (carried over from the previous excitation pulses). Equation (4) assumes that radiative recombination is dominated by bimolecular band-to-band recombination. We test this hypothesis by estimating the fraction of excitonic species for the material ($FAPbI_3$) studied in this work. We find that, for the excitation fluences used in our TRPL experiments ($<5\times10^{11}$ cm^{-2}), less than 3% of the photogenerated species are excitonic (see SI.2 in the Supplemental Material [36]). We also note that the exciton and free carrier population in poly(crystalline) semiconductors are considered as an equilibrium. Therefore, all charge carriers show free-carrier and exciton characteristics, but, in this case, are vastly dominated by their free carrier nature. Thus, Eq. (4) accurately described the radiative recombination for this work.

To be able to use Eq. (4), we first estimate $\Delta n(t,\ z)$ [and $\Delta p(t,\ z)$] by solving the one-dimensional diffusion equation numerically. Here, we use the Crank-Nicolson method [37,38] to estimate the charge-carrier density over time and space. It includes the vertical diffusion quantified through the ambipolar vertical charge-carrier mobility, μ_{vert}, inside the studied material, as well as the surface recombination velocities at the two interfaces, S_1 and S_2. The approach is a finite-difference method and is described in more detail in SI.3 in the Supplemental Material [36]. In short, at each point in time, diffusion is calculated based on the charge-carrier gradients throughout the film thickness and the mobility. Simultaneously, surface and bulk recombination are taken into account. The latter can be written as

$$\frac{\delta\Delta n(t,z)}{\delta t} = R_{\mathrm{NR,bulk}}(t,z) + R_{\mathrm{rad}}(t,z), \tag{5}$$

where $R_{\mathrm{NR,bulk}}$ is the nonradiative bulk recombination; R_{rad} is the radiative bulk recombination, as described in Eq. (4). For the charge-carrier densities that are typically reached during a TRPL experiment ($<10^{18}$ cm^{-3}), the impact of Auger recombination is negligible. An equivalent equation can be written for the change in hole density. $R_{\mathrm{NR,bulk}}$ here includes a shallow electron trap that is not recombination active, as well as a recombination-active deep trap. By symmetry, the model can also describe an equivalent hole trap by swapping n and p. Then, we use two coupled rate equations [39,40] (one for free electrons and one for trapped electrons; see SI.3 in the Supplemental Material [36]). This enables us to obtain information about k_{c} (the electron capture rate), k_{e} (the electron emission rate), and k_{d} (the nonradiative recombination rate). The inclusion of shallow defects in the recombination will impact the long-term photoluminescence decay via multiple trapping or detrapping events, or otherwise put, a significant component of the electron and hole density at longer times will be residing in shallow trap states, which have a long lifetime, reducing the free-carrier density and hence radiative decay rate [41,53]. Trapped charges can accumulate under pulsed excitation, with corresponding long-lived counter charges residing in the conduction or valance band states. A similar effect has been described, for example, by Trimpl *et al.* [13] and Kiligaridis *et al.* [54]. We mimic this effect via the equilibrium hole density, p_{eq}. It is nontrivial to calculate p_{eq} in the presence of shallow defects and diffusion and hence is made a variable parameter in our work.

The PL response can then be calculated via Eqs. (3) and (4). In SI.3 in the Supplemental Material [36], the impact of every parameter used in the model on the observed TRPL decay is summarized. From this, we determine a minimal set of measurements required to disentangle all effects: two excitation fluences (here, 4.8×10^{10} and 4.8×10^{11} cm^{-2}) from one side and at least one excitation fluence from the other side.

To test the validity of the model, we calculate the photogenerated charge-carrier density as a function of z coordinate throughout the perovskite thin-film thickness. We calculate $n(t,\ z)$ for different time points (0.1–10^4 ns) and different scenarios. In Fig. 2(a), we show the impact of diffusion without any recombination on the transient charge-carrier density distribution. The initial charge-carrier density follows an exponential distribution, in accordance with the absorption coefficient, α (here, approx. 3×10^5 cm^{-1} at the excitation wavelength of the laser of 405 nm), of the perovskite material. Over time, we observe that the charge-carrier density homogenizes throughout the thickness, because of diffusion, and stabilizes at approximately 15% of its initial peak value at $t=0$, $z=0$.

In Fig. 2(b), we include bulk recombination as well via Eq. (5) with a radiative recombination constant (k_{rad}) of 10^{-10} cm^3 s^{-1}, no shallow defect ($k_{\mathrm{c}}=k_{\mathrm{e}}=0$), k_{d} of 10^6 s^{-1}, and no surface recombination. While the initial redistribution of charge carriers also happens here, it does not stabilize after homogenization, but instead further decays with a charge-carrier-dependent recombination rate. In Fig. 2(c), we rerun the calculation, but this time the nonradiative bulk recombination is suppressed and instead the surface recombination at $z=0$ is set to 10^4 cm s^{-1}. This value is higher than most efficient systems relevant for photovoltaic applications (i.e., an unpassivated perovskite/C_{60} interface will typically have an surface recombination velocity (SRV) of $>10^3$ cm s^{-1}) chosen

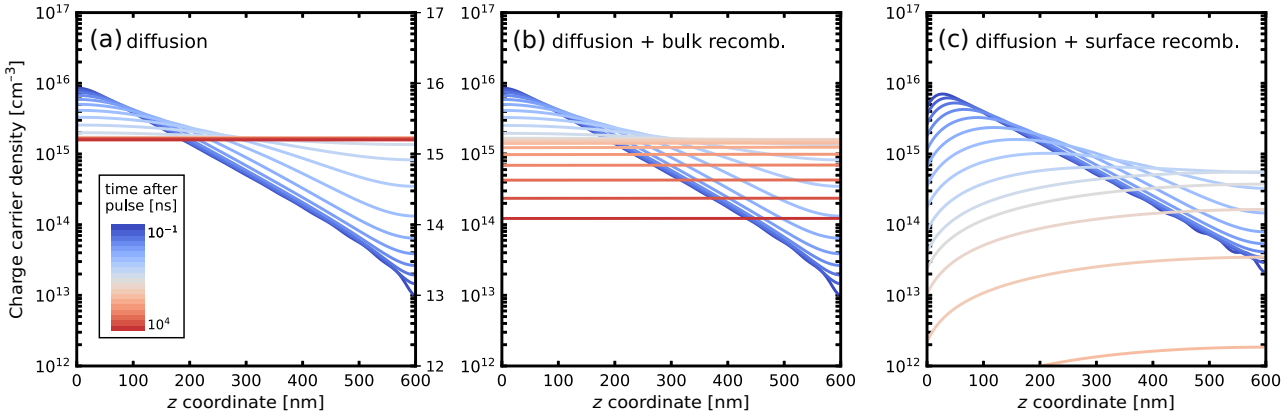

FIG. 2. Charge-carrier density calculated over time is shown as a function of the z coordinate throughout the thin-film thickness of 600 nm. Impact of (a) only diffusion, (b) diffusion and bulk recombination following Eq. (5), and (c) the combination of all processes happening simultaneously with a surface recombination of 10^4 cm s^{-1} at $z = 0$. In all cases, the color change from blue to red indicates increasing time.

here for illustration purposes. Due to this high surface recombination, the charge-carrier density never reaches a fully homogenized state, but instead is depleted towards the quenching surface. All three transient charge-carrier densities are consistent with our current understanding of the underlying physics. In the following, we use the model together with the Bayes-MCMC approach to infer all parameters and gain insights into the photophysics of perovskite thin films and half-stack stacks. Additionally, we include parameters that are specific to the dataset but are not material parameters. These include the noise floor of the PL data ($\varepsilon_{\mathrm{PL}}$) and the width of the Gaussian likelihood function. Additional information on these parameters is given in the Supplemental Material [36].

We would like to point out at this stage that the Bayes-MCMC approach, while powerful, is limited by the choice of physical model employed. As with any other methodology used to extract physically meaningful parameters from experimental data, the underlying physical model may not fully capture the real transient charge-carrier dynamics. This error will be directly carried forward by the inferred parameter values. For this work, we developed a model that could accurately fit our experimental data and was in line with the state-of-the-art understanding. In the following sections, the outcome of the Bayes-MCMC algorithm for different types of samples is interpreted with the awareness that the suitability of our model may change when new research and insights become available.

III. RESULTS

A. Understanding transient photoluminescence in a $FAPbI_3$ thin film

We use $FAPbI_3$ thin films as a model system to understand the functionality and limitation of the Bayes-MCMC methodology. The $FAPbI_3$ thin films studied here have been optimized to be used as an absorber in the negative-intrinsic-positive (n-i-p) solar cell architecture, but for this study, the films were fabricated on bare glass. A thin layer of Al_2O_3 nanoparticles was used on top of the glass to improve the wettability of the perovskite precursor solution and adhesion of the as-crystallized perovskite films (see SI.1 in the Supplemental Material [36] for details on the fabrication process).

We used a 398 nm (3.12 eV) picosecond pulsed excitation laser and illuminated the sample from the substrate and material sides (S_{bot} and S_{top}, respectively) to measure the sample (see SI.2 in the Supplemental Material [36] for experimental details). Two fluences (4.8×10^{10} and 4.8×10^{11} cm^{-2} per pulse) were used to disentangle different recombination pathways from reabsorption and diffusion. The deep-blue excitation source was used to induce a strong charge-carrier density concentration gradient throughout the film thickness at early times, which allowed inference of the charge-carrier diffusion in the z direction (as shown in Fig. 2). The simultaneous assessment of a complete dataset consisting of four individual measurements allows for the inference of all parameters of the physical model (described in SI.3 in the Supplemental Material [36] in more detail).

After running the Bayes-MCMC algorithm on a set of four TRPL decays for 2×10^3 steps (10^3 to tune the NUTS sampler and 10^3 to store values), we need to ascertain that the Markov chains have converged and are in a region of "good agreement" [high likelihood (L)] between the experimental and calculated TRPL decays. We therefore estimate the average negative $\ln(L)_{\mathrm{av}}$ via Eq. (S23) in the Supplemental Material [36] at every step of each individual Markov chain. $-\ln(L)_{\mathrm{av}}$ is the average $\ln(L)$ for each data point and is used to allow better comparability of the different samples assessed in this work (see SI.4 in the Supplemental Material [36] for details). A region of

good agreement corresponds to a region of low $-\ln(L)_{av}$, since "perfect" agreement results in $L=1$ and $\ln(L)=0$. In Fig. 3(a), we show $-\ln(L)_{av}$ at each step of the Markov chain and for each of the ten individual chains. The ten MCMC chains converge within 100 samples of tuning. We estimate the median $-\ln(L)_{av}$ of the final 10^3 drawn samples to be about 0.47. We then store the last 10^3 samples of each Markov chain for further calculations, analysis, and to build the parameter distributions shown in Fig. S9 in the Supplemental Material [36].

Next, we need to confirm that this high-likelihood region also corresponds to TRPL decay traces that closely match the experimental data. We thus show the median of the final 10^3 calculated TRPL decays ("median line") alongside the normalized experimental data (normalized to the measured intensity at $t=0$ ns) in Fig. 3(b). The median of the calculated TRPL decays agrees well with the measured ones across all timescales and all four measurements. It is worth mentioning that it is a great achievement for a single methodology and physical model to be able to describe the early- and late-time decay of the photoluminescence simultaneously and across two fluences and two illumination directions with such close agreement.

In addition to the calculated TRPL decays, we obtain the posterior probability distribution of each parameter (the inferred parameters are summarized in Table S1, and the distributions are shown in Fig. S9 in the Supplemental Material [36]) from the stored samples. Having probability distributions for each parameter has multiple advantages: it gives us quantifiably a level of certainty over the determination of a given parameter based on the data presented to the Bayes-MCMC, and it allows for non-Gaussian posterior parameter distributions to be observed. For instance, we may determine a wide spread of possible values for a parameter, indicating a low level of confidence or a low sensitivity of the TRPL decay to this parameter. It should be noted that this finding is quite powerful, since it allows us to understand if a parameter even impacts the observed data and report possible nonidentifiability [55] as such. Nonidentifiability of a parameter given a set of experimental data is a powerful statement and improves the transparency of scientific reports. Hence, we report all values as M (Q_1–Q_3), where M is the median and Q_1–Q_3 is the interquartile range. We also note that, even though we use a repetition rate of only 50 kHz here, a certain fraction of the trapped charges will live longer than that, especially in the presence of shallow defects. These lead to an effective "photodoping" density, p_{eq}, which we determine to be on the order of 10^{15} cm^{-3}, similar to values reported in other studies [23,53].

A parameter that we obtain from our modeling is the vertical mobility (μ_{vert}). We want to reemphasize here that the mobility we obtain is the ambipolar vertical mobility. Since radiative recombination requires the presence of both electrons and holes, and intensity is proportional to the product of the electron and hole number density, the reduction in the carrier density of either species will result in a reduction in PL intensity. Since the decay of the early-time PL signal is driven by the diffusion of charge carriers away from the surface and into the bulk, the subsequently derived mobilities should be limited by the fastest of the two charge-carrier species [23,53]. The value for μ_{vert} that we determine for our $FAPbI_3$ thin films is 4.1 (4.0–4.2) $\times 10^{-1}$ cm^2 (Vs)$^{-1}$. While this value seems relatively low, in comparison with mobility values derived from optical-pump terahertz-probe (OPTP) spectroscopy, later we compare it to the values obtained from other methods that probe longer-range charge transport and find good agreement.

We now compare the parameters related to bulk recombination inferred by the Bayes-MCMC approach with a more common least-squares fit of Eq. (1) (see SI.2 in the Supplemental Material [36] for details). For the least-squares fit, we obtain an average k_1 of 9.6×10^4 s^{-1} and a k_2 of 8.7×10^{-11} cm^3 s^{-1}. With our new approach, we obtained a radiative recombination rate, k_{rad}, of 7.5 (7.4–7.5) $\times 10^{-11}$ cm^3 s^{-1}. This value is the internal radiative recombination rate, as reported by others [56–58], and is close to the obtained k_2. From the parameters related to nonradiative bulk recombination (k_c, k_e, and k_d), we can estimate an effective recombination rate, $k_{NR,eff}$, using Eq. (S16) in the Supplemental Material [36]. We find a $k_{NR,eff}$ of 1.6 (0.9–2.1) $\times 10^4$ s^{-1}. The discrepancy between k_1 and $k_{NR,eff}$ is related to the assumptions of the models they respectively derive from: k_1 is the monomolecular recombination rate and is assumed to be constant over the entire decay, while $k_{NR,eff}$ is impacted by trapping or detrapping events.

Since $k_{NR,eff}$ does not agree well with k_1, we look at the surface recombination, which also impacts the steady-state nonradiative recombination rate. We thus convert the obtained SRVs from our Bayes-MCMC estimations into surface recombination rates. Assuming that the total SRV is constant over the time of the measurement, the surface nonradiative recombination rate can be calculated via [34]

$$k_{NR,S_i} = \frac{S_i}{d}, \tag{6}$$

where d is the film thickness. We show $k_{NR,S}$ for both S_{top} and S_{bot} alongside the calculated $k_{NR,eff}$ in Fig. S5 within the Supplemental Material [36]. Both are within a factor of 2 of the extracted k_1. As is logical after considering the nonradiative recombination pathways, k_1 obtained from Eq. (1) contains information on both the surface and bulk recombination but cannot disentangle the two. The Bayes-MCMC approach enables us to derive information about both effects separately, which is even more important when we study device half-stacks later.

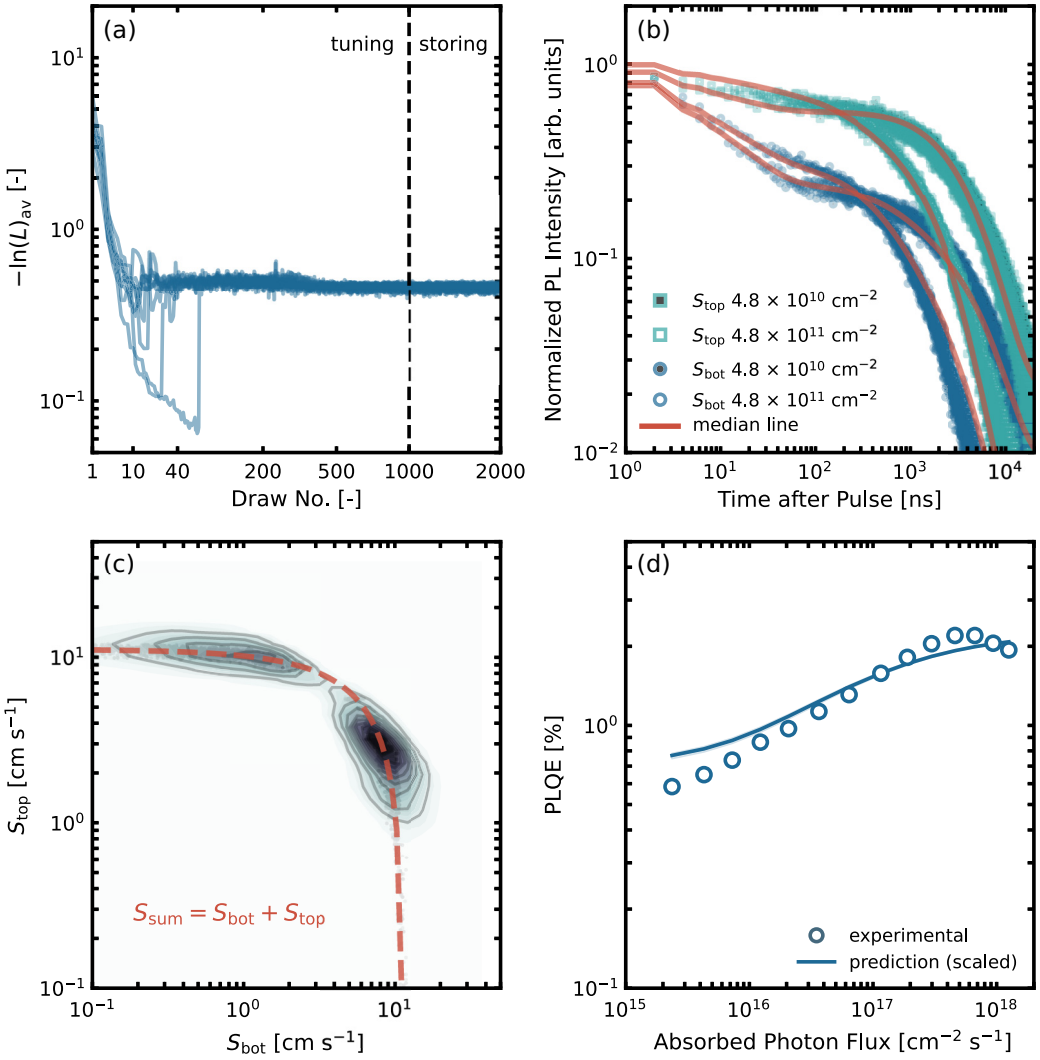

FIG. 3. (a) Negative $\ln(L)_{av}$ for the $FAPbI_3$ sample assessed here as a function of the sample number along 10 individual Markov chains (shown as individual lines). Lower the negative $\ln(L)_{av}$, the better the agreement between data and model. First 10^3 samples are used to tune the NUTS sampler and second 10^3 samples are stored. (b) Set of TRPL data measured from the substrate (S1) and perovskite (S2) sides for two fluences (4.8×10^{10} and 4.8×10^{11} cm^{-2}) each. Data are normalized to the initial number of PL counts ($t = 0$ ns). Lines indicate the median TRPL calculated from the last 10^3 samples of the 10 Markov chains ("median line"). (c) Two surface recombination velocities (S_{top} and S_{bot}) are shown in a 2D corner plot. Darker the color, the higher the likelihood of this region. Faint gray spots indicate the underlying sample values. Dashed line follows $S_{sum} = S_{top} + S_{bot}$. (d) Intensity-dependent PLQE, with the measured (empty circles) and calculated scaled (lines) values shown. PLQE is calculated for 500 random samples out of the 10^3 stored parameter sets (to reduce the calculation time) and the median (solid line) and Q_1–Q_3 range (shaded area) is shown.

While it is useful by itself to obtain estimates for all of these parameters, the Bayes-MCMC approach also allows for more in-depth analysis of the data. We first demonstrate this here by looking more closely at the early-time decay in Fig. 3(b). The photoluminescence decays faster when the sample is excited from the substrate side (S_{bot}). It was postulated in a previous study [59] that this was a result of charge-carrier diffusion and a higher SRV at S_{bot}. Here, the full physical model, together with the Bayesian inference algorithm, allows us to test this hypothesis more rigorously. In Fig. S9 within the Supplemental Material [36], we do not find a significantly higher value for S_{bot}. However, since the Markov chains have ended up in a region of high likelihood, we can also learn something about the correlation of S_{bot} and S_{top}, the discrete surface recombination velocities at the two surfaces. A two-dimensional (2D) plot is shown in Fig. 3(c), where the darker color indicates higher probability. The plot is symmetric about a diagonal line, behavior that had been previously reported by Fai *et al.* for the case of one-sided illumination [23]. We find two solutions, which cluster around the limiting cases of $S_{top} \approx S_{sum}$ or $S_{bot} \approx S_{sum}$.

For the thin film on glass, neither of the two solutions is clearly favored; however, we see later that this changes when interfacial recombination between the perovskite and a transport layer is considered. This analysis exemplifies how the complex interplay of a number of parameters generates the TRPL decay.

To further confirm the validity of the physical model and the Bayes-MCMC method, and its relevance to steady-state conditions, we used the derived parameters to reproduce intensity-dependent PLQE measurements. During the PLQE measurement, the samples were illuminated from the substrate side with a 445 nm (2.76 eV) continuous-wave laser. It is a steady-state measurement, where the PL response of the sample depends on the ratio of radiative and nonradiative recombination for any given photogenerated population of charge carriers. The PL of the sample is collected in an integrating sphere using a spectrograph (see note SI.2 in the Supplemental Material [36] for details). The measured PLQE values are shown as empty circles in Fig. 3(d). We can calculate the outcome of this experiment from the parameter distributions we have obtained from the TRPL Bayes-MCMC simulation. In short, we solved Eq. (5) for the steady-state condition under continuous-wave illumination to obtain the steady-state charge-carrier density, n_{SS}. The internal PLQE ($\eta_{QE,int}$) is then defined as

$$\eta_{QE,int} = \frac{k_{rad} n_{SS} p_{SS}}{G}, \tag{7}$$

where G is the charge-carrier generation rate (see SI.2 in the Supplemental Material [36] for more details). Here, $p_{SS} = n_{SS} + p_{eq}$, as described in a previous study [60]. We calculate $\eta_{QE,int}$ for 500 random parameter draws and then take the median and Q_1–Q_3 from them. $\eta_{QE,int}$ can be much higher than the measured external PLQE ($\eta_{QE,ext}$), due to total internal reflection (low escape probability) or parasitic absorption [56]. We thus scale the calculated PLQE to the measured data (we show the unscaled PLQE in Fig. S2 within the Supplemental Material [36]). We closely replicate the slope of the PLQE [solid line and shaded area in Fig. 3(d)] across all absorbed photon fluxes. This further substantiates our physical model, as well as validating the Bayes-MCMC approach.

B. Disentangling surface and bulk recombination in device half-stacks

After having validated the Bayes-MCMC method with neat $FAPbI_3$ thin films on glass, we now explore its ability to derive information from device half-stacks, where the perovskite absorber forms an interface with a charge-transport layer. Here, we assess the interfaces SnO_2-$FAPbI_3$ (here "SnO_2") and $FAPbI_3$-Spiro-OMeTAD (here "Spiro-OMeTAD"), which are common in the regular *n-i-p* architecture. The fabrication details are summarized in SI.1 in the Supplemental Material [36], but, in short, the SnO_2 layer was fabricated as a TiO_2-SnO_2 bilayer and Spiro-OMeTAD was doped with 4-*tert*-butylpyridine, lithium bis(trifluoromethanesulfonyl)imide (Li-TFSI), and cobalt bis(trifluoromethanesulfonyl)imide (Co-TFSI), as commonly used to achieve improved conductivity of the transport layer and optimized efficiency in *n-i-p* solar cell devices.

We followed the same methodology from the first experiment, where each sample was illuminated from the substrate side with two fluences (4.8×10^{10} and 4.8×10^{11} cm^{-2}), but this time only the higher fluence could be measured sufficiently for the illumination from the top side. The resulting experimental data and calculated median TRPL decay of the last 10^3 steps of the ten Markov chains are shown in Fig. 4(a) for SnO_2 and Spiro-OMeTAD (all inferred parameters are summarized in Table S1 and histograms for all parameters are shown in Figs. S10 and S11 within the Supplemental Material [36]).

A long PL decay can be observed for the SnO_2 sample, while for the Spiro-OMeTAD sample, the PL intensity is quickly quenched over the first few hundred nanoseconds for all fluences. The latter was previously reported and ascribed to a high interfacial recombination rate at the perovskite-Spiro-OMeTAD interface [31]. In both cases, the calculated median TRPL decay describes the experimental data sufficiently well.

We proceed to investigate how interface and bulk recombination are affected by the transport layers. In contrast to other reports, the Bayes-MCMC algorithm can clearly disentangle the two interfaces for the SnO_2 and Spiro-OMeTAD samples. This is very powerful, since it allows us to study the effects of both surfaces and the bulk of the absorber on the overall recombination and resulting TRPL decay, and hence, reveals any changes that may occur in the bulk as a consequence of processing on the different underlying layers or the impact of additives in subsequent layers.

We determine surface recombination velocities of 9 (4–17) $cm\,s^{-1}$ for the SnO_2-$FAPbI_3$ interface [3 (1–7) $cm\,s^{-1}$ for $FAPbI_3$-air] and 1300 (1200–1400) $cm\,s^{-1}$ for the $FAPbI_3$-Spiro-OMeTAD interface [100 (60–120) $cm\,s^{-1}$ for glass-$FAPbI_3$]. For comparison, we previously determined 4 (2–10) $cm\,s^{-1}$ for $FAPbI_3$-air and 7 (1–9) $cm\,s^{-1}$ for the glass-$FAPbI_3$ interface. The SRVs at both interfaces are well comparable to values reported for other perovskite-based half-stacks: 11–270 $cm\,s^{-1}$ for the TiO_2-SnO_2-PVSK interface [31], and 1400–4200 $cm\,s^{-1}$ for the PVSK-Spiro-OMeTAD$_{doped}$ interface [31,61–63]. The increased SRV of the Spiro-OMeTAD sample at the glass-$FAPbI_3$ interface is unexpected, but it may be due to the impact of additives in the Spiro-OMeTAD solution [64].

To study the impact of the interface and bulk, we again use Eq. (6) to estimate $k_{NR,S}$ for the perovskite-transport layer interfaces. We then compare these values to the bulk

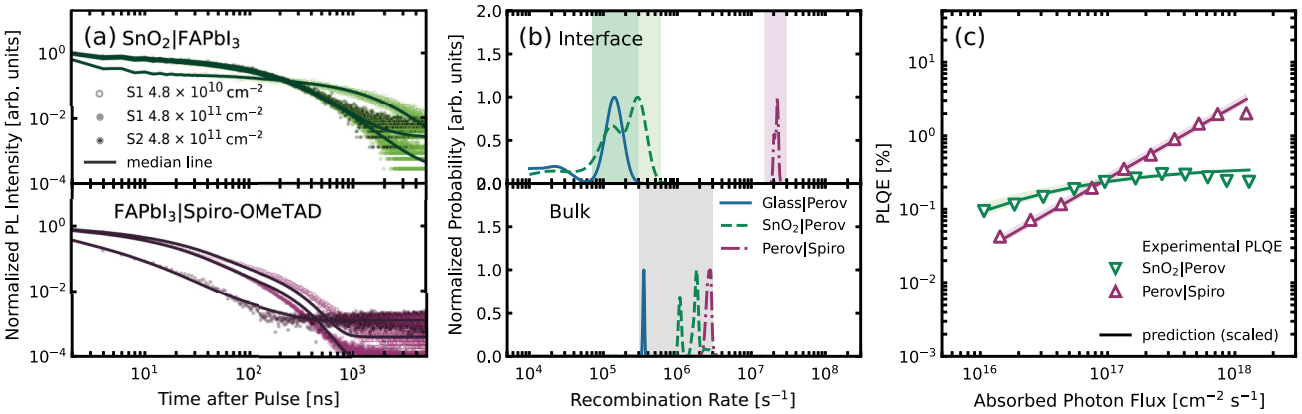

FIG. 4. TRPL decays of half-devices of (a) SnO_2-$FAPbI_3$ and (b) $FAPbI_3$-Spiro-OMeTAD measured from the substrate (S1) and perovskite (S2) sides with two excitation fluences (4.8×10^{10} and 4.8×10^{11} cm^{-2}). Data are normalized to the initial number of PL counts ($t = 0$ ns). (b) Surface (top) and bulk (bottom) nonradiative recombination rates are compared in the same plot for all samples. (c) Experimental (shapes) and calculated scaled (lines) intensity-dependent PLQEs for the half-devices are shown. For the calculated PLQE, 500 random samples out of the 10^3 stored parameters were used.

recombination rate, which is defined as

$$k_{\text{bulk}}(\Delta n) = k_{\text{NR,eff}} + k_{\text{rad}} \Delta n p_{\text{eq}}, \tag{8}$$

where $k_{\text{NR,eff}}$ is obtained from Eq. (S16) in the Supplemental Material [36]. We evaluate Eq. (8) at the initial photogenerated charge-carrier density equivalent to one sun illumination intensity ($\Delta n_{1\text{sun}} \approx 2.5 \times 10^{15}$ cm^{-3} under our 50 kHz pulsed excitation). The perovskite-transport layer surface ($k_{\text{NR},S}$) and bulk (k_{bulk}) recombination constants are shown side by side in Fig. 4(b). For the $FAPbI_3$ thin film on glass, we derive a k_{bulk} value of 3.5 (3.4–3.6) $\times 10^5$ s^{-1} and a $k_{\text{NR},S}$ value of 1.2 (0.2–1.5) $\times 10^5$ s^{-1}. Both recombination rates are among the lowest reported values in the literature and have been associated with high device performance [31,65,66]. It explicitly indicates that the bulk and surface recombination processes contribute equally to electron-hole recombination, i.e., recombination in the isolated thin films is not surface dominated. We determine k_{bulk} values of 1.8 (1.1–1.8) $\times 10^6$ and 2.7 (2.5–2.8) $\times 10^6$ s^{-1}, as well as $k_{\text{NR},S}$ values of 1.4 (0.6–2.8) $\times 10^5$ and 2.2 (2.1–2.3) $\times 10^7$ s^{-1} for the perovskite interface with SnO_2 and Spiro-OMeTAD samples, respectively. This analysis can be used to understand that performance losses in a photovoltaic device would stem from the interfaces, as they change significantly in the half-stacks, but there is also a nonzero contribution from changes in bulk recombination.

Again, we estimate the intensity-dependent PLQE for these two samples using Eqs. (7) and (S4) in the Supplemental Material [36] and compare the results with experimental data. The measured PLQE data are shown in Fig. 4(c) for both samples as empty triangles. As expected, we observe a reduced PLQE for both the SnO_2 and Spiro-OMeTAD samples with respect to the $FAPbI_3$ thin films on glass. In addition, both half-stacks show a steeper slope of the intensity-dependent PLQE increase. This has been linked to enhanced interfacial recombination (and increased ideality factor) [67]. Alongside the experimental data, we show the median of the simulated PLQE as a solid line and the interquartile range as shaded area in Fig. 4(c). Again, we needed to scale the calculated internal PLQE to match the experimental external PLQE values. Still, we can reproduce the slope of the intensity-dependent PLQE with good accuracy for both samples (see SI.2 in the Supplemental Material [36] for details and the unscaled PLQE). For the SnO_2 sample, there is still a remaining discrepancy at higher intensities, indicating that there are additional nonradiative decay mechanisms, which are not included in our current physical model. For instance, a recent report [68] suggested this was due to filling of surface traps, which limited the PLQE at higher excitation photon fluxes. This would mean that interface recombination at perovskite-transport layer interfaces would have to be described by a model similar to the "shallow defect" model used here for nonradiative bulk recombination. Then, the effects of charge reinjection and surface trap filling could be taken into account. This is part of ongoing work and goes beyond the scope of the work presented here.

C. Device-relevant vertical mobility

One of the most advantageous aspects of the present work is the ability to derive an estimation of the vertical charge-carrier mobility (here μ_{vert}) in device-relevant thin films, with quantified error. The vertical, or out-of-plane, substrate direction is the one relevant for operating photovoltaic devices and light-emitting diodes. We find median values for μ_{vert} of 4.1 (4.0–4.2) $\times 10^{-1}$, 2.2 (0.8–2.4) $\times 10^0$,

and 1.3 (1.2–1.7) $\times 10^{-1}$ cm^2 (Vs)$^{-1}$ for the $FAPbI_3$ thin film on glass, the SnO_2 sample, and when coated with Spiro-OMeTAD, respectively. For the last two, this parameter is usually not easily accessible by other techniques. For instance, electronic measurements can be significantly influenced if the mobility or conductivity within the transport layer is comparable to the perovskite.

As a confirmation of the result, the shift of the photoluminescence spectrum over time can also be used to extract a vertical mobility, μ_{vert}. Following photoexcitation of charge carriers, the electron and hole density is a maximum near the illuminated surface. As the charge carriers diffuse into the film away from the surface, electron and hole band-to-band recombination leads to PL being generated deeper and deeper into the film. This leads to a redshift of the photoluminescence spectra, due to self-absorption of emitted light, which preferentially absorbs the higher energy photons [69]. Following recent work [42], we used our TCSPC setup (see SI.2 in the Supplemental Material [36] for details) and measured the TRPL decay of a similar $FAPbI_3$ thin film on glass with a 405 nm excitation wavelength. We changed the detection wavelength to be larger or smaller than 808 nm (the central wavelength of the PL peak) within $\pm$100 nm and determined the PL shift by calculating the following ratio:

$$r_{PL}(t) = \frac{\sum_{\lambda>808\ nm} PL(\lambda, t)}{\sum_{\lambda<808\ nm} PL(\lambda, t)} - 1. \quad (9)$$

We show the results in Fig. 5(a). Following Cho *et al.*, we fit $r_{PL}(t)$ using the same diffusion model we formulated for the TRPL data above to independently determine μ_{vert} for the $FAPbI_3$ thin film on glass. Through this, we fit the relative shift in PL with the diffusion coefficient as the sole variable, following pulsed excitation. The fitting curves are shown in Fig. 5(a) as solid lines. The extracted mobility is 0.42 (0.40–0.46) cm^2 (Vs)$^{-1}$, which is very close to the values that we obtained from the Bayes-MCMC approach, giving us high confidence in our extracted parameters.

We then compare the mobility values obtained from the Bayes-MCMC method with the measurement of electronic contact based transient photoconductivity (TPC) [43,72]. For the TPC measurements, we used a similar $FAPbI_3$ thin film on glass to that used for the TRPL measurement (three in total for statistical purposes) and evaporated 80-nm-thick interdigitated gold electrodes with a 300 μm channel width on the top (see SI.2 in the Supplemental Material [36] for details). The samples were illuminated with a 550 nm (2.25 eV) 10 Hz pulsed laser from the substrate side to induce approximately homogeneous charge-carrier generation throughout the sample thickness. The technique yields the photoconductivity in the in-plane direction (with respect to the substrate) from which the sum of the lateral mobilities of electrons and holes ($\Sigma\mu_{lat}$) can be estimated, which we have identified to be relevant to "long-range" (tens of nm to microns) transport. In a recent report [72], we showed how to obtain a μ_{lat} value that was largely independent of charge-carrier density, and hence, allowed us to estimate this parameter with high accuracy. We also showed that the TPC method yielded values similar to the often-employed time-resolved microwave conductivity (TRMC). In Fig. 5(b), we show the estimated mobilities as a function of excitation fluence. We obtain a $\Sigma\mu_{lat}$ value of 2.7 (2.1–3.7) $\times 10^{-1}$ cm^2 (Vs)$^{-1}$ for the $FAPbI_3$ thin film on glass. Notably, this is comparable to our μ_{vert} estimated from our new Bayes-MCMC approach. It is important to reemphasize here that lateral and vertical mobility are defined by the direction of charge-carrier transport with respect to the underlying substrate and are not necessarily related to the crystallographic planes of the perovskite material.

In Fig. 5(c), we show all mobilities obtained from the different methods side by side. We compare them to values obtained for $FAPbI_3$ single crystals through pulsed space-charge-limited current measurements [73,74] and mobility measurements obtained using OPTP [75] techniques. The latter typically probes charge conduction in perovskites over a length scale of a few to tens of nanometers. Both mobilities are in the range of 27–40 cm^2 (Vs)$^{-1}$ for $FAPbI_3$. We observed a similar difference previously, when comparing "short-range" OPTP measurements with in-plane long-range TPC measurements on different three-dimensional perovskites [43,72]. Here, the mobility determined from charge-carrier transport in the vertical direction (the direction relevant for photovoltaic devices) is still much lower than the short-range mobility determined by OPTP spectroscopy, but around a factor of about 3 larger than the long-range in-plane mobility obtained via TPC.

This finding is crucial, since it is common practice in the field to use the high mobility from single-crystal measurements, together with a measurement of the PL decay lifetime (from TRPL), to estimate the diffusion length of charge carriers within the perovskite material [76], especially when performing drift-diffusion simulations of perovskite-based photovoltaic devices [70,71,77]. If the results shown here are representative, then this approach would lead to an overestimation of the diffusion length. Similar mobilities for the vertical charge-carrier transport in perovskite materials were reported previously [10,12] but were never highlighted as being comparatively low. Using our obtained vertical mobility values, we estimate a diffusion length in the range of 2 μm for all the samples in this work. This is still long enough not to impact the device performance significantly for most perovskite-based devices, although PbSn-based narrow-band-gap devices need thicknesses close to 1 μm to achieve suitably high short-circuit currents [78,79] and often struggle to reach current densities of the detailed balance limit [80]. It will also be interesting to understand, in

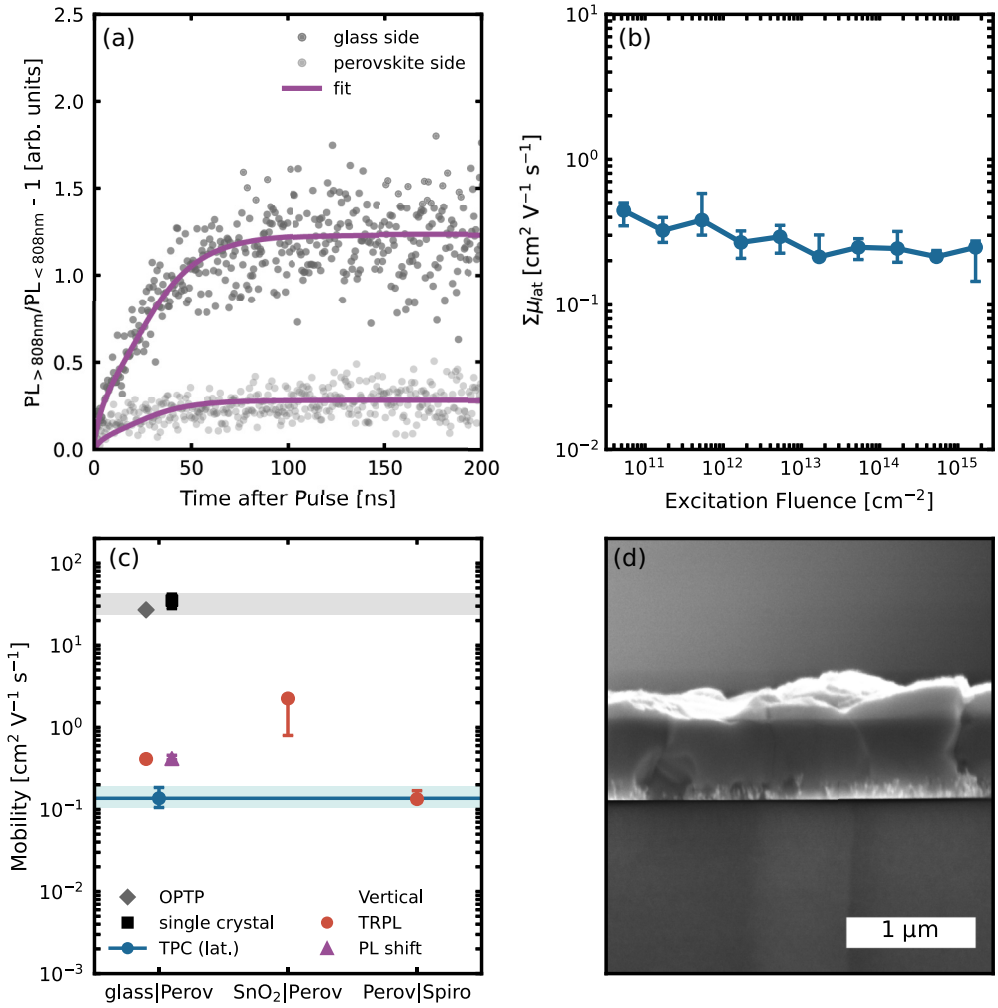

FIG. 5. (a) Spectral shift of the photoluminescence spectrum is estimated by the ratio of the PL above 808 nm and the PL below 808 nm (808 nm was the peak of the emission). Results are shown for measurements from the glass and perovskite sides. Purple lines indicate the fit, as described in SI.2 in the Supplemental Material [36]. (b) Calculated mobilities from the TPC measurements as a function of excitation fluence are shown. (c) Extracted mobilities from all methods used in this work are shown side by side, as well as a literature value for the $FAPbI_3$ material from OPTP [70] spectroscopy and a single-crystal measurement [71]. As the mobility values obtained from TPC are $\Sigma\mu$, we show half of that value (assuming $\mu_n = \mu_p$) for better comparability. Values obtained from TPC are measured laterally and over longer distances than the OPTPT measurements. All error bars in this figure are the interquartile range shown with the median. (d) Cross-section SEM image of the $FAPbI_3$ thin film on glass is shown to illustrate the high material quality. Single grains can be seen throughout the entire thickness.

future studies, what fraction of the losses due to long-term degradation originate from transport losses.

It is still not clear what the origin of the observed discrepancy between the vertical single crystal (or OPTP) and longer range TPC mobility is, even though many reports have seen similarly low values, when estimating diffusion in the vertical direction [10,12,69,81–83]. A recent study [84] combining optical-pump terahertz-probe spectroscopy, time-resolved microwave conductivity, and photoluminescence measurements speculated that the differences might stem from the presence of grain boundaries appearing throughout the thickness of the perovskite thin film.

To investigate this further, we took cross-section SEM images of the $FAPbI_3$ thin film on glass. One representative image is shown in Fig. 5(d), where large grains visible in the SEM images span the entire thickness of the thin film. We therefore speculate that the reduction in mobility must come from intragrain defects, which would then be greatly reduced in single crystals. Recent work on CdSeTe thin films [44] has shown that a reduction in mobility over time can also stem from trapping and detrapping events in the presence of shallow traps, and this may also be applicable to our system. The change in vertical mobility for the SnO_2 and Spiro-OMeTAD samples, as shown in Fig. 5(c), may then be interpreted, for instance, as being

due to different crystallization or additional defect formation. At this point, the origin of the intragrain (as observed in the SEM images) traps is not known. More and more reports show that the grains from SEM are again divided into smaller regions, with different local orientation [85–88], PbI_2 inclusions [89], ferroelectric domains [90], or the presence of intragrain impurities [91]. It will need to be the focus of future research to investigate the nature and origin of these traps or scattering defects within the grains.

The lower mobility estimated from the TPC measurements, as compared to μ_{vert} we estimate here, must originate from scattering centers or planes on a longer distance scale than the film thickness, which are likely to originate from scattering from grain boundaries, in addition to intragrain defects.

IV. CONCLUSIONS

In this work, we have combined Bayesian inference with a MCMC algorithm to realize a powerful methodology to extract physically meaningful parameters from experimental data of metal halide perovskites. We used TRPL, an often employed and common measurement technique, and a physical model based on previously reported theory to infer up to 8 material- and sample-specific parameters (μ_{vert}, k_c, k_e, k_d, k_{rad}, S_{top}, S_{bot}, and p_{eq}). After verifying the approach with a $FAPbI_3$ thin film on glass, we assessed half-stack structures with SnO_2 and Spiro-OMeTAD as electron- and hole-transporting materials, respectively. Via previously applied methods, it was difficult to assess these structures directly, due to interfacial recombination and substrate-dependent perovskite crystallinity [32,92,93]. From our methodology presented here, we could infer all parameters for these structures, with corresponding estimated levels of certainty.

One important finding is that the mobility value for vertical charge-carrier transport is lower in magnitude than the values obtained from short-range techniques (from OPTP spectroscopy or single-crystal measurements) and closer to those from the long-range techniques (TPC or TRMC). Our understanding is that this is the relevant mobility value for understanding and describing real perovskite-based optoelectronic devices, which are composed of polycrystalline thin films and where charge transport is in the vertical direction. As such, we expect that our Bayes-MCMC approach will be employed to help accelerate the development of perovskite-based optoelectronic devices, such as solar cells and light-emitting diodes. Furthermore, we hope that the methodology will be extended to other techniques, where a multitude of parameters govern the outcome of an optoelectronic measurement, and other materials.

ACKNOWLEDGMENTS

The authors acknowledge funding from the Engineering and Physical Science Research Council (EPSRC) UK under Grants No. EP/V010840/1 and No. EP/T025077/1. M.K.C. expressed his gratitude to the Deutsche Forschungsgemeinschaft for financial support via the SPP2196 Priority Program (CH 1672/3-1). A.D. would like to thank the Penrose scholarship for funding his studentship. S.S. thanks the EPSRC UK for support under Grant No. EP/V010840/1. F.M.R. was funded by the EPSRC UK under Grant No. EP/S516119/1. D.P.M. acknowledges financial support from Marie Skłodowska-Curie Actions Grant Agreement No. SAMA 101029896, a program grant funded by EPSRC ATIP (Grant No. EP/T028513/1), and HEFSPV (Grant No. EP/V027131/1). H.J. acknowledges support through sponsorships from Oxford PV.

M.K.C., A.D., and H.J.S. conceived the project. M.K.C. carried out the material characterization studies and conducted the modeling. A.D. measured the ellipsometry of the samples presented. A.D. and F.M.R. helped optimize the Bayesian inference algorithm. S.S. fabricated all samples shown in this work. D.P.M. provided useful suggestions for the paper. H.J. recorded the cross-section SEM images. M.K.C. and A.D. prepared the manuscript under the supervision of H.J.S. All authors revised and proofed the written manuscript.

H.J.S. is a co-founder and Chief Scientific Officer of Oxford PV, a company commercializing perovskite solar cells.

DATA AVAILABILITY

The data that support the findings of this article are openly available [94,95], embargo periods may apply.

[1] H. Min, D. Y. Lee, J. Kim, G. Kim, K. S. Lee, J. Kim, M. J. Paik, Y. K. Kim, K. S. Kim, M. G. Kim, T. J. Shin, and S. I. Seok, Perovskite solar cells with atomically coherent interlayers on SnO_2 electrodes, Nature **598**, 444 (2021).

[2] W. Peng, K. Mao, F. Cai, H. Meng, Z. Zhu, T. Li, S. Yuan, Z. Xu, X. Feng, J. Xu, M. D. McGehee, and J. Xu, Reducing nonradiative recombination in perovskite solar cells with a porous insulator contact, Science **379**, 683 (2023).

[3] S. Zhang, *et al.*, Minimizing buried interfacial defects for efficient inverted perovskite solar cells, Science **380**, 404 (2023).

[4] S. Hu, K. Otsuka, R. Murdey, T. Nakamura, M. A. Truong, T. Yamada, T. Handa, K. Matsuda, K. Nakano, A. Sato, K. Marumoto, K. Tajima, Y. Kanemitsu, and A. Wakamiya, Optimized carrier extraction at interfaces for 23.6% efficient tin–lead perovskite solar cells, Energy Environ. Sci. **15**, 2096 (2022).

[5] M. Stolterfoht, C. M. Wolff, J. A. Márquez, S. Zhang, C. J. Hages, D. Rothhardt, S. Albrecht, P. L. Burn, P. Meredith, T. Unold, and D. Neher, Visualization and suppression of interfacial recombination for high-efficiency large-area pin perovskite solar cells, Nat. Energy **3**, 847 (2018).

[6] A. Dasgupta, S. Mahesh, P. Caprioglio, Y.-H. Lin, K.-A. Zaininger, R. D. J. Oliver, P. Holzhey, S. Zhou, M. M. McCarthy, J. A. Smith, M. Frenzel, M. G. Christoforo, J. M. Ball, B. Wenger, and H. J. Snaith, Visualizing macroscopic inhomogeneities in perovskite solar cells, ACS Energy Lett. **7**, 2311 (2022).

[7] P. Caprioglio, J. A. Smith, R. D. J. Oliver, A. Dasgupta, S. Choudhary, M. D. Farrar, A. J. Ramadan, Y.-H. Lin, M. G. Christoforo, J. M. Ball, J. Diekmann, J. Thiesbrummel, K.-A. Zaininger, X. Shen, M. B. Johnston, D. Neher, M. Stolterfoht, and H. J. Snaith, Open-circuit and short-circuit loss management in wide-gap perovskite *p-i-n* solar cells, Nat. Commun. **14**, 932 (2023).

[8] L. Krückemeier, B. Krogmeier, Z. Liu, U. Rau, and T. Kirchartz, Understanding Transient Photoluminescence in halide perovskite layer stacks and solar cells, Adv. Energy Mater. **11**, 2003489 (2021).

[9] A. A. B. Baloch, F. H. Alharbi, G. Grancini, M. I. Hossain, Md. K. Nazeeruddin, and N. Tabet, Analysis of photocarrier dynamics at interfaces in perovskite solar cells by time-resolved photoluminescence, J. Phys. Chem. C **122**, 26805 (2018).

[10] S. D. Stranks, G. E. Eperon, G. Grancini, C. Menelaou, M. J. P. Alcocer, T. Leijtens, L. M. Herz, A. Petrozza, and H. J. Snaith, Electron-hole diffusion lengths exceeding 1 micrometer in an organometal trihalide perovskite absorber, Science **342**, 341 (2013).

[11] G. Vidon, S. Cacovich, M. Legrand, D. Ory, D. Suchet, J.-B. Puel, and J.-F. Guillemoles, in *2021 Ieee 48th Photovolt Specialists Conf Pvsc* (2021), pp. 0150–0153.

[12] A. Bercegol, F. J. Ramos, A. Rebai, T. Guillemot, D. Ory, J. Rousset, and L. Lombez, Slow diffusion and long lifetime in metal halide perovskites for photovoltaics, J. Phys. Chem. C **122**, 24570 (2018).

[13] M. J. Trimpl, A. D. Wright, K. Schutt, L. R. V. Buizza, Z. Wang, M. B. Johnston, H. J. Snaith, P. Müller-Buschbaum, and L. M. Herz, Charge-carrier trapping and radiative recombination in metal halide perovskite semiconductors, Adv. Funct. Mater. **30**, 2004312 (2020).

[14] G. Kang, J.-S. Yoon, G.-W. Kim, K. Choi, T. Park, R.-H. Baek, and J. Lim, Electron trapping and extraction kinetics on carrier diffusion in metal halide perovskite thin films, J. Mater. Chem. A **7**, 25838 (2019).

[15] M. Taddei, S. Jariwala, R. J. E. Westbrook, S. Gallagher, A. C. Weaver, J. Pothoof, M. E. Ziffer, H. J. Snaith, and D. S. Ginger, Interpreting halide perovskite semiconductor photoluminescence kinetics, ACS Energy Lett. **9**, 2508 (2024).

[16] J. Chen, J. Lv, X. Liu, J. Lin, and X. Chen, A study on theoretical models for investigating time-resolved photoluminescence in halide perovskites, Phys. Chem. Chem. Phys. **25**, 7574 (2023).

[17] J. I. H. Haggar, S. S. Ghataora, V. Trinito, J. Bai, and T. Wang, Study of the luminescence decay of a semipolar green light-emitting diode for visible light communications by time-resolved electroluminescence, ACS Photonics **9**, 2378 (2022).

[18] G. Han, H. D. Hadi, A. Bruno, S. A. Kulkarni, T. M. Koh, L. H. Wong, C. Soci, N. Mathews, S. Zhang, and S. G. Mhaisalkar, Additive selection strategy for high performance perovskite photovoltaics, J. Phys. Chem. C **122**, 13884 (2018).

[19] W. Chen, N. D. Pham, H. Wang, B. Jia, and X. Wen, Spectroscopic insight into efficient and stable hole transfer at the perovskite/spiro-OMeTAD interface with alternative additives, ACS Appl. Mater. Interfaces **13**, 5752 (2021).

[20] K. P. Chiu, The influence of a trap state on the photoluminescence decay times under single pulse excitation, Opt. Quantum Electron. **55**, 163 (2023).

[21] T. Bayes, An essay towards solving a problem in the doctrine of chances, Biometrika **45**, 296 (1958).

[22] O. Abril-Pla, V. Andreani, C. Carroll, L. Dong, C. J. Fonnesbeck, M. Kochurov, R. Kumar, J. Lao, C. C. Luhmann, O. A. Martin, M. Osthege, R. Vieira, T. Wiecki, and R. Zinkov, PyMC: A modern, and comprehensive probabilistic programming framework in Python, PeerJ Comput. Sci. **9**, e1516 (2023).

[23] C. Fai, A. J. C. Ladd, and C. J. Hages, Machine learning for enhanced semiconductor characterization from time-resolved photoluminescence, Joule **6**, 2585 (2022).

[24] C. Fai, C. J. Hages, and A. J. C. Ladd, Rapid optoelectronic characterization of semiconductors by combining Bayesian inference with metropolis sampling, PRX Energy **2**, 033013 (2023).

[25] C. P. Robert and G. Casella, Monte Carlo statistical methods, Springer Texts Stat. **7**, 267 (2004).

[26] M. D. Hoffman and A. Gelman, The no-U-turn sampler: Adaptively setting path lengths in Hamiltonian Monte Carlo, J. Mach. Learn. Res. **15**, 1593 (2014).

[27] Y. Yang, M. Yang, D. T. Moore, Y. Yan, E. M. Miller, K. Zhu, and M. C. Beard, Top and bottom surfaces limit carrier lifetime in lead iodide perovskite films, Nat. Energy **2**, 16207 (2017).

[28] H. Chen, *et al.*, Regulating surface potential maximizes voltage in all-perovskite tandems, Nature **613**, 676 (2023).

[29] R. D. J. Oliver, P. Caprioglio, F. Peña-Camargo, L. R. V. Buizza, F. Zu, A. J. Ramadan, S. G. Motti, S. Mahesh, M. M. McCarthy, J. H. Warby, Y.-H. Lin, N. Koch, S. Albrecht, L. M. Herz, M. B. Johnston, D. Neher, M. Stolterfoht, and H. J. Snaith, Understanding and suppressing non-radiative losses in methylammonium-free wide-bandgap perovskite solar cells, Energy Environ. Sci. **15**, 714 (2021).

[30] T. Kirchartz, J. A. Márquez, M. Stolterfoht, and T. Unold, Photoluminescence-based characterization of halide perovskites for photovoltaics, Adv. Energy Mater. **10**, 1904134 (2020).

[31] J. Wang, W. Fu, S. Jariwala, I. Sinha, A. K. Jen, Y. Ginger, and D. S, Reducing surface recombination velocities at the electrical contacts will improve perovskite photovoltaics, ACS Energy Lett. **4**, 222 (2019).

[32] M. D. Bastiani, V. D'Innocenzo, S. D. Stranks, H. J. Snaith, and A. Petrozza, Role of the crystallization substrate on the photoluminescence properties of organo-lead mixed halides perovskites, APL Mater. **2**, 081509 (2014).

[33] K. P. Goetz and Y. Vaynzof, The challenge of making the same device twice in perovskite photovoltaics, ACS Energy Lett. **7**, 1750 (2022).

[34] M. Maiberg and R. Scheer, Theoretical study of time-resolved luminescence in semiconductors. II. Pulsed excitation, J. Appl. Phys. **116**, 123711 (2014).

[35] M. Maiberg, T. Hölscher, S. Zahedi-Azad, and R. Scheer, Theoretical study of time-resolved luminescence in semiconductors. III. Trap states in the band gap, J. Appl. Phys. **118**, 105701 (2015).

[36] See the Supplemental Material http://link.aps.org/supplemental/10.1103/PRXEnergy.4.013001 for additional information about the experimental methods, details about the inference algorithm, the physical model, and probability distributions for all inferred parameters. It also includes Refs. [23,24,35,37–52].

[37] J. Crank and P. Nicolson, A practical method for numerical evaluation of solutions of partial differential equations of the heat-conduction type, Adv. Comput. Math. **6**, 207 (1996).

[38] G. Walther, The Crank-Nicolson method implemented from scratch in PYTHON. At https://github.com/waltherg/georio_fastpages/_notebooks/2013-12-03-Crank_Nicolson.ipynb.

[39] J. G. Simmons and G. W. Taylor, Nonequilibrium steady-state statistics and associated effects for insulators and semiconductors containing an arbitrary distribution of traps, Phys. Rev. B **4**, 502 (1970).

[40] W. Shockley and W. T. Read, Statistics of the recombinations of holes and electrons, Phys. Rev. **87**, 835 (1952).

[41] Y. Yuan, G. Yan, C. Dreessen, T. Rudolph, M. Hülsbeck, B. Klingebiel, J. Ye, U. Rau, and T. Kirchartz, Shallow defects and variable photoluminescence decay times up to 280 µs in triple-cation perovskites, Nat. Mater. **23**, 1 (2024).

[42] C. Cho, S. Feldmann, K. M. Yeom, Y.-W. Jang, S. Kahmann, J.-Y. Huang, T. C. Yang, M. N. T. Khayyat, Y.-R. Wu, M. Choi, J. H. Noh, S. D. Stranks, and N. C. Greenham, Efficient vertical charge transport in polycrystalline halide perovskites revealed by four-dimensional tracking of charge carriers, Nat. Mater. **21**, 1388 (2022).

[43] M. Kober-Czerny, S. G. Motti, P. Holzhey, B. Wenger, J. Lim, L. M. Herz, and H. J. Snaith, Excellent long-range charge-carrier mobility in 2D perovskites, Adv. Funct. Mater. **32**, 2203064 (2022).

[44] D. Kuciauskas, M. Nardone, A. Bothwell, D. Albin, C. Reich, C. Lee, and E. Colegrove, Why increased CdSeTe charge carrier lifetimes and radiative efficiencies did not result in voltage boost for CdTe solar cells, Adv. Energy Mater. **13**, 2301784 (2023).

[45] J. C. de Mello, H. F. Wittmann, and R. H. Friend, An improved experimental determination of external photoluminescence quantum efficiency, Adv. Mater. **9**, 230 (1997).

[46] R. J. Elliott, Intensity of Optical Absorption by Excitons, Phys. Rev. **108**, 1384 (1957).

[47] C. L. Davies, M. R. Filip, J. B. Patel, T. W. Crothers, C. Verdi, A. D. Wright, R. L. Milot, F. Giustino, M. B. Johnston, and L. M. Herz, Bimolecular recombination in methylammonium lead triiodide perovskite is an inverse absorption process, Nat. Commun. **9**, 293 (2018).

[48] M. Cirelli, T. Hambye, P. Panci, M. al, Aoki, T. Toma, A. V. Chen, J. Liang, Z.-L. Wu, and Y.-L. Astropart, Self-consistent calculation of the Sommerfeld enhancement, J. Cosmol. Astropart. Phys. **2016**, 021 (2016).

[49] C. L. Davies, J. Borchert, C. Q. Xia, R. L. Milot, H. Kraus, M. B. Johnston, and L. M. Herz, Impact of the organic cation on the optoelectronic properties of formamidinium lead triiodide, J. Phys. Chem. Lett. **9**, 4502 (2018).

[50] M. N. Saha, On a physical theory of stellar spectra, Proc. R. Soc. London, Ser. A **99**, 135 (1921).

[51] J. Pan, Z. Chen, T. Zhang, B. Hu, H. Ning, Z. Meng, Z. Su, D. Nodari, W. Xu, G. Min, M. Chen, X. Liu, N. Gasparini, S. A. Haque, P. R. F. Barnes, F. Gao, and A. A. Bakulin, Operando dynamics of trapped carriers in perovskite solar cells observed via infrared optical activation spectroscopy, Nat. Commun. **14**, 8000 (2023).

[52] A. Gelman, J. B. Carlin, H. S. Stern, D. B. Dunson, A. Vehtari, and D. B. Rubin, *Bayesian Data Analysis* (Chapman & Hall/CRC, New York, 2014).

[53] C. J. Hages, A. Redinger, S. Levcenko, H. Hempel, M. J. Koeper, R. Agrawal, D. Greiner, C. A. Kaufmann, and T. Unold, Identifying the real minority carrier lifetime in nonideal semiconductors: A case study of kesterite materials, Adv. Energy Mater. **7**, 1700167 (2017).

[54] A. Kiligaridis, P. A. Frantsuzov, A. Yangui, S. Seth, J. Li, Q. An, Y. Vaynzof, and I. G. Scheblykin, Are Shockley-Read-Hall and *ABC* models valid for lead halide perovskites?, Nat. Commun. **12**, 3329 (2021).

[55] A. Sjölander and S. Vansteelandt, Frequentist versus Bayesian approaches to multiple testing, Eur. J. Epidemiol. **34**, 809 (2019).

[56] J. M. Richter, M. Abdi-Jalebi, A. Sadhanala, M. Tabachnyk, J. P. H. Rivett, L. M. Pazos-Outón, K. C. Gödel, M. Price, F. Deschler, and R. H. Friend, Enhancing photoluminescence yields in lead halide perovskites by photon recycling and light out-coupling, Nat. Commun. **7**, 13941 (2016).

[57] P. Fassl, V. Lami, F. J. Berger, L. M. Falk, J. Zaumseil, B. S. Richards, I. A. Howard, Y. Vaynzof, and U. W. Paetzold, Revealing the internal luminescence quantum efficiency of perovskite films via accurate quantification of photon recycling, Matter **4**, 1391 (2021).

[58] T. W. Crothers, R. L. Milot, J. B. Patel, E. S. Parrott, J. Schlipf, P. Müller-Buschbaum, M. B. Johnston, and L. M. Herz, Photon reabsorption masks intrinsic bimolecular charge-carrier recombination in $CH_3NH_3PbI_3$ perovskite, Nano Lett. **17**, 5782 (2017).

[59] P. Zeng, G. Feng, X. Cui, and M. Liu, Revealing the role of interfaces in photocarrier dynamics of perovskite films by alternating front/back side excitation time-resolved photoluminescence, J. Phys. Chem. C **124**, 6290 (2020).

[60] S. Feldmann, S. Macpherson, S. P. Senanayak, M. Abdi-Jalebi, J. P. H. Rivett, G. Nan, G. D. Tainter, T. A. S. Doherty, K. Frohna, E. Ringe, R. H. Friend, H. Sirringhaus, M. Saliba, D. Beljonne, S. D. Stranks, and F. Deschler, Photodoping through local charge carrier accumulation in alloyed hybrid perovskites for highly efficient luminescence, Nat. Photonics **14**, 123 (2020).

[61] P. Mäkinen, F. Fasulo, M. Liu, G. K. Grandhi, D. Conelli, B. Al-Anesi, H. Ali-Löytty, K. Lahtonen, S. Toikkonen, G. P. Suranna, A. B. Muñoz-García, M. Pavone, R. Grisorio, and P. Vivo, Less is more: Simplified fluorene-based dopant-free hole transport materials promote the long-term ambient

stability of perovskite solar cells, Chem. Mater. **35**, 2975 (2023).

[62] M. Liu, S. Dahlström, C. Ahläng, S. Wilken, A. Degterev, A. Matuhina, M. Hadadian, M. Markkanen, K. Aitola, A. Kamppinen, J. Deska, O. Mangs, M. Nyman, P. D. Lund, J.-H. Smått, R. Österbacka, and P. Vivo, Beyond hydrophobicity: How F4-TCNQ doping of the hole transport material improves stability of mesoporous triple-cation perovskite solar cells, J. Mater. Chem. A **10**, 11721 (2022).

[63] D. W. deQuilettes, J. J. Yoo, R. Brenes, F. U. Kosasih, M. Laitz, B. D. Dou, D. J. Graham, K. Ho, Y. Shi, S. S. Shin, C. Ducati, M. G. Bawendi, and V. Bulović, Reduced recombination via tunable surface fields in perovskite thin films, Nat. Energy **9**, 457 (2024).

[64] Z. Li, C. Xiao, Y. Yang, S. P. Harvey, D. H. Kim, J. A. Christians, M. Yang, P. Schulz, S. U. Nanayakkara, C.-S. Jiang, J. M. Luther, J. J. Berry, M. C. Beard, M. M. Al-Jassim, and K. Zhu, Extrinsic ion migration in perovskite solar cells, Energy Environ. Sci. **10**, 1234 (2017).

[65] Y. Yang, Y. Yan, M. Yang, S. Choi, K. Zhu, J. M. Luther, and M. C. Beard, Low surface recombination velocity in solution-grown $CH_3NH_3PbBr_3$ perovskite single crystal, Nat. Commun. **6**, 7961 (2015).

[66] Y. Shi, E. Rojas-Gatjens, J. Wang, J. Pothoof, R. Giridharagopal, K. Ho, F. Jiang, M. Taddei, Z. Yang, E. M. Sanehira, M. D. Irwin, C. Silva-Acuña, and D. S. Ginger, (3-Aminopropyl)trimethoxysilane surface passivation improves perovskite solar cell performance by reducing surface recombination velocity, ACS Energy Lett. **7**, 4081 (2022).

[67] P. Caprioglio, C. M. Wolff, O. J. Sandberg, A. Armin, B. Rech, S. Albrecht, D. Neher, and M. Stolterfoht, On the origin of the ideality factor in perovskite solar cells, Adv. Energy Mater. **10**, 2000502 (2020).

[68] R. L. Chin, A. M. Soufiani, P. Fassl, J. Zheng, E. Choi, A. Ho-Baillie, U. W. Paetzold, T. Trupke, and Z. Hameiri, Surface saturation current densities of perovskite thin films from Suns-photoluminescence quantum yield measurements, Prog. Photovoltaics **33**, 109 (2024).

[69] B. Wenger, P. K. Nayak, X. Wen, S. V. Kesava, N. K. Noel, and H. J. Snaith, Consolidation of the optoelectronic properties of $CH_3NH_3PbBr_3$ perovskite single crystals, Nat. Commun. **8**, 590 (2017).

[70] S. R. Hosseini, M. Bahramgour, P. Y. Sefidi, A. T. Mashayekh, A. Moradi, N. Delibas, M. G. Hosseini, and A. Niaei, Investigating the effect of non-ideal conditions on the performance of a planar $CH_3NH_3PbI_3$-based perovskite solar cell through SCAPS-1D simulation, Heliyon **8**, e11471 (2022).

[71] P. K. Patel, Device simulation of highly efficient eco-friendly $CH_3NH_3SnI_3$ perovskite solar cell, Sci. Rep. **11**, 3082 (2021).

[72] J. Lim, M. Kober-Czerny, Y.-H. Lin, J. M. Ball, N. Sakai, E. A. Duijnstee, M. J. Hong, J. G. Labram, B. Wenger, and H. J. Snaith, Long-range charge carrier mobility in metal halide perovskite thin-films and single crystals via transient photo-conductivity, Nat. Commun. **13**, 4201 (2022).

[73] A. A. Zhumekenov, M. I. Saidaminov, M. A. Haque, E. Alarousu, S. P. Sarmah, B. Murali, I. Dursun, X.-H. Miao, A. L. Abdelhady, T. Wu, O. F. Mohammed, and O. M. Bakr, Formamidinium lead halide perovskite crystals with unprecedented long carrier dynamics and diffusion length, ACS Energy Lett. **1**, 32 (2016).

[74] E. A. Duijnstee, *et al.*, Understanding the degradation of methylenediammonium and its role in phase-stabilizing formamidinium lead triiodide, J. Am. Chem. Soc. **145**, 10275 (2023).

[75] W. Rehman, R. L. Milot, G. E. Eperon, C. Wehrenfennig, J. L. Boland, H. J. Snaith, M. B. Johnston, and L. M. Herz, Charge-carrier dynamics and mobilities in formamidinium lead mixed-halide perovskites, Adv. Mater. **27**, 7938 (2015).

[76] G. Hodes and P. V. Kamat, Understanding the implication of carrier diffusion length in photovoltaic cells, J. Phys. Chem. Lett. **6**, 4090 (2015).

[77] M. Stolterfoht, P. Caprioglio, C. M. Wolff, J. A. Márquez, J. Nordmann, S. Zhang, D. Rothhardt, U. Hörmann, Y. Amir, A. Redinger, L. Kegelmann, F. Zu, S. Albrecht, N. Koch, T. Kirchartz, M. Saliba, T. Unold, and D. Neher, The impact of energy alignment and interfacial recombination on the internal and external open-circuit voltage of perovskite solar cells, Energy Environ. Sci. **12**, 2778 (2019).

[78] D. Zhao, Y. Yu, C. Wang, W. Liao, N. Shrestha, C. R. Grice, A. J. Cimaroli, L. Guan, R. J. Ellingson, K. Zhu, X. Zhao, R.-G. Xiong, and Y. Yan, Low-bandgap mixed tin–lead iodide perovskite absorbers with long carrier lifetimes for all-perovskite tandem solar cells, Nat. Energy **2**, 17018 (2017).

[79] Z. Yang, Z. Yu, H. Wei, X. Xiao, Z. Ni, B. Chen, Y. Deng, S. N. Habisreutinger, X. Chen, K. Wang, J. Zhao, P. N. Rudd, J. J. Berry, M. C. Beard, and J. Huang, Enhancing electron diffusion length in narrow-bandgap perovskites for efficient monolithic perovskite tandem solar cells, Nat. Commun. **10**, 4498 (2019).

[80] O. Almora, *et al.*, Device performance of emerging photovoltaic materials (version 4), Adv. Energy Mater. **14**, 2303173 (2024).

[81] G. Xing, N. Mathews, S. Sun, S. S. Lim, Y. M. Lam, M. GraážŮzel, S. Mhaisalkar, and T. C. Sum, Long-range balanced electron-and hole-transport lengths in organic-inorganic $CH_3NH_3PbI_3$, Science **342**, 344 (2013).

[82] A. Bou, H. ÄĂboliņš, A. Ashoka, H. Cruanyes, A. Guerrero, F. Deschler, and J. Bisquert, Extracting *in situ* charge carrier diffusion parameters in perovskite solar cells with light modulated techniques, ACS Energy Lett. **6**, 2248 (2021).

[83] M. C. Gélvez-Rueda, N. Renaud, and F. C. Grozema, Temperature dependent charge carrier dynamics in formamidinium lead iodide perovskite, J. Phys. Chem. C **121**, 23392 (2017).

[84] H. Hempel, *et al.*, Predicting solar cell performance from terahertz and microwave spectroscopy, Adv. Energy Mater. **12**, 2102776 (2022).

[85] S. Jariwala, H. Sun, G. W. P. Adhyaksa, A. Lof, L. A. Muscarella, B. Ehrler, E. C. Garnett, and D. S. Ginger, Local crystal misorientation influences non-radiative recombination in halide perovskites, Joule **3**, 3048 (2019).

[86] M. U. Rothmann, J. S. Kim, J. Borchert, K. B. Lohmann, C. M. O'Leary, A. A. Sheader, L. Clark, H. J. Snaith, M. B. Johnston, P. D. Nellist, and L. M. Herz, Atomic-scale

microstructure of metal halide perovskite, Science **370**, 548 (2020).

[87] W. Liu, Y. Liu, J. Wang, C. Wu, C. Liu, L. Xiao, Z. Chen, S. Wang, and Q. Gong, Twin domains in organometallic halide perovskite thin-films, Crystals **8**, 216 (2018).

[88] L. A. Muscarella, E. M. Hutter, S. Sanchez, C. D. Dieleman, T. J. Savenije, A. Hagfeldt, M. Saliba, and B. Ehrler, Crystal orientation and grain size: Do they determine optoelectronic properties of $MAPbI_3$ perovskite?, J. Phys. Chem. Lett. **10**, 6010 (2019).

[89] A. Alberti, C. Bongiorno, E. Smecca, I. Deretzis, A. L. Magna, and C. Spinella, Pb clustering and PbI_2 nanofragmentation during methylammonium lead iodide perovskite degradation, Nat. Commun. **10**, 2196 (2019).

[90] A. D. Schulz, M. O. Schmitt, M. Braun, A. Colsmann, M. Hinterstein, and H. Röhm, Ferroelectricity and crystal phases in mixed-cation lead iodide perovskite solar cells, Sol. RRL **6**, 2200808 (2022).

[91] S. Cai, Z. Li, Y. Zhang, T. Liu, P. Wang, M.-G. Ju, S. Pang, S. P. Lau, X. C. Zeng, and Y. Zhou, Intragrain impurity annihilation for highly efficient and stable perovskite solar cells, Nat. Commun. **15**, 2329 (2024).

[92] A. Al-Ashouri, M. Marčinskas, E. Kasparavičius, T. Malinauskas, A. Palmstrom, V. Getautis, S. Albrecht, M. D. McGehee, and A. Magomedov, Wettability improvement of a carbazole-based hole-selective monolayer for reproducible perovskite solar cells, ACS Energy Lett. **8**, 898 (2023).

[93] S. Chen, X. Dai, S. Xu, H. Jiao, L. Zhao, and J. Huang, Stabilizing perovskite-substrate interfaces for high-performance perovskite modules, Science **373**, 902 (2021).

[94] M. Kober-Czerny, A. Dasgupta, S. Seo, F. Rombach, D. McMeekin, H. Jin, and H. J. Snaith, Supporting Data for: "Determining Material Parameters of Metal Halide Perovskites Using Time-resolved Photoluminescence, Zenodo, 2024, http://doi.org/10.5281/zenodo.14231027.

[95] M. Kober-Czerny, manuelkoberczerny/assessing-TRPL-with-bayesian-inference and-MCMC: Paper_acceptance_release (initial_release), Zenodo, 2024, http://doi.org/10.5281/zenodo.14535086